Micromechanical IBARs: Tunable High-Q Resonators for Temperature-Compensated Reference Oscillators

Gavin K. Ho, *Member, IEEE*, Krishnakumar Sundaresan, *Member, IEEE*, Siavash Pourkamali, *Member, IEEE*, and Farrokh Ayazi, *Senior Member, IEEE*

Abstract—This paper presents a unique capacitive micromechanical resonator and oscillator architecture for temperature-compensated frequency references. The I-shaped bulk acoustic resonator (IBAR) is designed to have excellent electrical tunability for temperature compensation (TC) and dynamic frequency control. High quality factor and low motional resistance are also achieved. The applicable range of frequencies is 1–30 MHz, in which quality factors exceeding 100 000 have been measured. Resonator metrics, including the electrostatic tuning coefficient, normalized dynamic stiffness, and relative dynamic compliance, are introduced. A small-signal resistance in the resonator is reported and explained. This unexpected resistance is beneficial for oscillator functionality over a large temperature range. The interface IC, inclusive of all blocks for sustaining oscillations and TC, is also presented. A two-chip 6-MHz oscillator with a temperature stability of 39 ppm over 100 °C is demonstrated. The interface IC consumes 1.9 mW. [2008-0166]

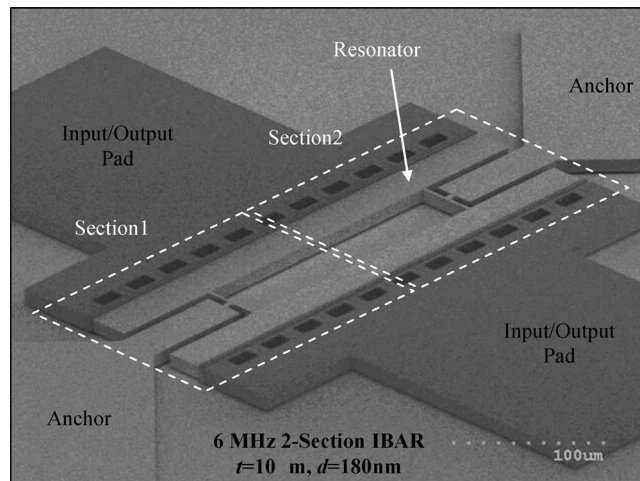*Index Terms*—Electrostatic devices, microelectromechanical devices, microresonators, Q factor, tunable oscillators, tuning.

Fig. 1. SEM of a 10-μm-thick two-section IBAR with conservative 180-nm gaps fabricated using the HARPSS-on-SOI process.

I. INTRODUCTION

FREQUENCY references are ubiquitous in electronics. In medium- to high-performance applications, quartz crystal units are the default solution since they provide excellent temperature stability, high quality factor Q, good linearity, and excellent long-term stability. However, the size of quartz crystal units and its manufacturing disparity to semiconductors are unattractive in many applications.

G. K. Ho was with the Micromachined Products Division, Analog Devices, Inc., Cambridge, MA 02139 USA, and also with the School of Electrical and Computer Engineering, Georgia Institute of Technology, Atlanta, GA 30332 USA. He is now with ParibX, Inc., Mountain View, CA 94040 USA (e-mail: gavinho@ieee.org).

K. Sundaresan was with the School of Electrical and Computer Engineering, Georgia Institute of Technology, Atlanta, GA 30332 USA. He is now with GE Global Research, Niskayuna, NY 12309 USA.

S. Pourkamali was with the School of Electrical and Computer Engineering, Georgia Institute of Technology, Atlanta, GA 30332 USA. He is now with the Department of Electrical and Computer Engineering, University of Denver, Denver, CO 80208 USA.

F. Ayazi is with the School of Electrical and Computer Engineering, Georgia Institute of Technology, Atlanta, GA 30332 USA.

Color versions of one or more of the figures in this paper are available online at http://ieeexplore.ieee.org.

Digital Object Identifier 10.1109/JMEMS.2010.2044866

Micromechanical resonators, particularly those fabricated from bulk materials such as single-crystal silicon (SCS), are ideal to displace quartz in low-power small-form-factor applications. See Fig. 1. Silicon is attractive as a structural material since it is well characterized, its material quality is tightly controlled, it intrinsically has low acoustic loss, and the crystalline structure has potential for low aging. Furthermore, capacitive transduction (i.e., electrostatic actuation and capacitive detection) enables a monolithic resonator body that has lower loss and better long-term stability than composite structures.

Low-power small-form-factor temperature-stable oscillators remain elusive despite the recent progress in micromechanical resonators [1]–[5]. Various schemes have been demonstrated to compensate for the -23- to -30-ppm/°C temperature dependence [6] of silicon resonators. Temperature compensation (TC) is necessary to improve the temperature stability. Geometric stress compensation [7], [8] is possible, but severe constraints are placed on resonator design. The time- and temperature-dependent stresses in the device and package will likely be problematic with that approach. Another technique is the addition of silicon dioxide (having positive temperature coefficient) [9]–[11]. Additional loss mechanisms that reduce resonator Q are introduced, however. Commercially available MEMS-based oscillators use fractional-N phase-locked loop (PLL) synthesizers [12], [13] to compensate for the temperature
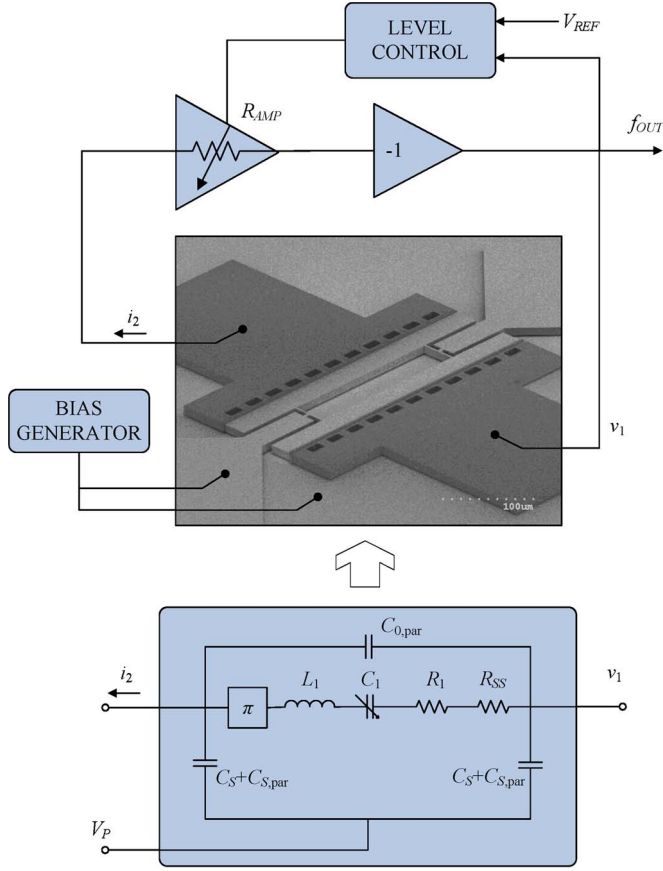
Fig. 2.   Oscillator architecture for TC and low-power operation, including a simplified electrical equivalent circuit of a symmetric IBAR.

dependence. The compromise with the fractional-N solution is added cost and complexity of electronics and high current consumption. Yet, another approach is oven control [14], [15], which is limited to applications with power budgets of 50 mW or more.

Electrostatic TC with automatic polarization voltage (V_P) correction is a new solution. V_P-correction is attractive because no additional structural features are necessary, the structures are monolithic, and the current consumption is far less than fractional-N PLL and oven control solutions. The tuning mechanism is inherent in capacitive resonators, and it also enables dynamic frequency control.

The focus of this paper is the high-Q tunable I-shaped bulk acoustic resonator (IBAR)[1] [16]. See Fig. 1. The fundamentals of oscillator stability, capacitive resonator modeling, and electrostatic tuning are briefly described. The IBAR geometry, its characteristics, and the design metrics follow next. The fabrication process and measurement data from a 6-MHz IBAR are described in the main article.[2] Finally, a brief description of the oscillator architecture (Fig. 2), the IC design [17], the measured temperature stability, and the measured phase noise are presented.

II. RESONATOR DESIGN AND MODELING

Oscillator stability and the basic characteristics of capacitive micromechanical resonators are presented first. The review facilitates a discussion on the IBAR design concepts. The IBAR is compared to other resonators in the same frequency space. Resonator metrics, such as the electrostatic tuning coefficient, normalized dynamic stiffness, and relative dynamic compliance, are introduced and described.

A. Oscillator Stability

One aspect of oscillator stability is the temperature dependence of its center frequency f_0

$$f_0 = f_0(f_s) \tag{1}$$

$$f_s = f_s(f_n). \tag{2}$$

f_0, pursuant to the phase requirement of the Barkhausen criterion, is dependent on f_s and f_n of the resonator, which are the resonant frequency of the motional arm and the undamped natural frequency, respectively. f_n can be approximated by

$$f_n \approx \frac{A_n}{L_{\text{gen}}} v_a \tag{3}$$

in which L_{gen} is a generalized frequency-defining dimension, A_n is a dimensionless parameter, $v_a = (E_i/\rho_m)^{0.5}$ is the acoustic velocity, E_i is the elastic modulus, and ρ_m is the mass density. The fractional temperature dependence of f_n is given by

$$\gamma_T \equiv \frac{1}{f_n} \frac{\partial f_n}{\partial T} = -\alpha_L + \frac{1}{v_a} \frac{dv_a}{dT} \tag{4}$$

in which α_L is the linear thermal expansion coefficient and T is the temperature. Quartz is unique in that some crystalline orientations have equal negating components of γ_T at certain temperatures [18]. With a one-dimensional (1-D) assumption, it can be shown that γ_T simplifies to[3]

$$\gamma_T = \frac{1}{2}(\alpha_L + \alpha_E) \tag{5}$$

where α_E is the fractional temperature dependence of the elastic modulus. In general, both α_L and α_E are temperature dependent. In most materials, the temperature dependence of f_n must be compensated for a stable oscillator f_0.

Another aspect of oscillator stability is phase noise. A modification of Leeson's model gives the following expression for the single-sideband phase noise [19], [20]:

$$L = \left[1 + \left(\frac{f_0}{2Q_L} \right)^2 \frac{1}{f_m^2} \right] \left[b_1 f_m^{-1} + \frac{Fk_BT}{P_R} \right]. \tag{6}$$

The square brackets on the right contain the amplifier flicker noise $b_1 f_m^{-1}$ and thermal noise floor Fk_BT/P_R. P_R, the resonator absorbed (and delivered) power, is important for a low noise floor. In (6), F is the noise figure, k_B is Boltzmann's

---

constant, T is the absolute temperature, f_m is the modulation frequency, and b_1 is the flicker coefficient. The left set of square brackets contains the loop transfer function that upconverts the amplifier noise at small f_m from the carrier. A high loaded Q in the resonator (Q_L) is critical for low close-to-carrier noise for this reason. In modern electronic systems, clock frequencies are typically synthesized from the reference oscillator. Since the transfer functions of such synthesizers have a low-pass characteristic (thereby filtering far-from-carrier noise), high Q_L is particularly important.

B. Capacitive Resonator Basics

In the simplified electrical equivalent model for a symmetric resonator (Fig. 2), the motional arm contains the motional resistance R_1, inductance L_1, capacitance C_1, and series resistance R_{SS}. Because the mode is symmetric, the phase shift of the motional current is π. The motional parameters are given by [4]

$$R_1 = \frac{k_n}{\omega_n Q_U \eta^2} \tag{7}$$

$$L_1 = \frac{m_n}{\eta^2} \tag{8}$$

$$C_1 = \frac{\eta^2}{k_{\text{tot}}} \tag{9}$$

in which k_n is the dynamic stiffness, ω_n is the angular natural frequency, Q_U is the unloaded quality factor, m_n is the dynamic mass, k_{tot} is the total dynamic stiffness, and η is the electromechanical coupling coefficient. Q_U can be considered as the mechanical quality factor, whereas Q_L is the electrically loaded quality factor (i.e., $Q_L \leq Q_U$). For a parallel-plate resonator, the linearized η is given by

$$\eta \approx V_{Pi} \frac{\varepsilon A_e}{d^2}. \tag{10}$$

The bias potential $V_{Pi} = V_P - V_{Bi}$ is the difference between the potential of the resonator body V_P and the potential of the fixed electrodes V_{Bi}, where $i = 1, \ldots$ is the fixed electrode number. In (10), ε is the permittivity, A_e is the electrode overlap area, and d is the size of the capacitive gap. The ability to build up and sustain oscillations is dependent on overcoming the motional resistance

$$R_1 = \frac{k_n d^4}{\omega_n Q_U V_{Pi}^2 \varepsilon^2 A_e^2}. \tag{11}$$

C. Electrostatic Tuning

Fine electrical tuning is provided through the tunable total dynamic stiffness given by

$$k_{\text{tot}} = k_n + \sum_i k_{ei} \tag{12}$$

in which k_{ei} is the polarization-dependent electrical stiffness from fixed electrode i. (Since k_{tot} is tunable, C_1 is shown as a tunable capacitance in Fig. 2.) The displacement-linearized electrical stiffness from fixed electrode i is

$$k_{ei,0} = -\frac{V_{Pi}^2 \varepsilon A_e}{d^3} \tag{13}$$

where A_e is the overlap area in one set of electrodes. For $\Delta f_e = f_s - f_n$, $f_s = 1/2\pi \cdot (L_1 C_1)^{-1/2}$, and $f_n = 1/2\pi \cdot (k_n/m_n)^{1/2}$, the fractional frequency tuning is given by

$$\frac{\Delta f_e}{f_n} \approx \frac{\sum_i k_{ei,0}}{2k_n}. \tag{14}$$

In most cases, $k_{ei,0} \ll k_n$. For a device with two fixed electrodes at the same potential

$$\frac{\Delta f_e}{f_n} \approx -\frac{\varepsilon A_e}{k_n d^3} V_{Pi}^2. \tag{15}$$

Since A_e, k_n, and gap size vary between designs, the electrostatic tuning coefficient γ_e is defined

$$\gamma_e \equiv \frac{\Delta f_e}{f_n} \frac{1}{V_{Pi}^2} = -\frac{\varepsilon A_e}{k_n d^3} \quad [\text{V}^{-2}]. \tag{16}$$

This parameter allows the tunability of various resonator topologies to be easily evaluated and compared. To increase electrostatic tuning, the gap size and normalized dynamic stiffness k_n/A_e must be minimized.[4]

Electrostatic tuning is the best method to control the frequency of a capacitive resonator. Traditionally, quartz resonator tuning or "pulling" is done via an external tunable capacitor. Since the typical C_1 for capacitive resonators is much less than 1 fF, resonator pulling via auxiliary capacitances is less effective than electrostatic tuning.

D. IBAR Concept

A suitable resonator for reference oscillators must have high Q[5] and low R_1 and provide a means for TC. The first two objectives should be familiar to the resonator designer. High Q is provided through symmetry and anchoring at low-velocity locations. Low R_1 is achieved by a large electrode area. For TC, sufficient electrostatic tuning is required.

Various forms of micromechanical resonators have been described in the literature. The variety includes rigid-body devices [21], [22], flexural beams [23], [24], disks [25], [26], and plates [5]. Rigid-body devices and flexural beams are electrostatically tunable since they have low k_n/A_e. However, at frequencies greater than 1 MHz [23], the size of the beam is greatly reduced, and R_1 consequently increases. Also, the Q of beams at 1 MHz and above is limited by anchor losses [27], [28]. Alternatively, disks and plates can have exceptional Q at higher frequencies. However, the k_n/A_e of these modes is large (i.e., the attainable electrical stiffness at modest bias voltages is relatively insignificant).

---

[4]For tuning and R_1, the normalized dynamic stiffness k_n/A_e is of utmost importance rather than the absolute dynamic stiffness.

[5]Q, when unspecified as being unloaded or loaded, refers to the unloaded mechanical quality factor by default.
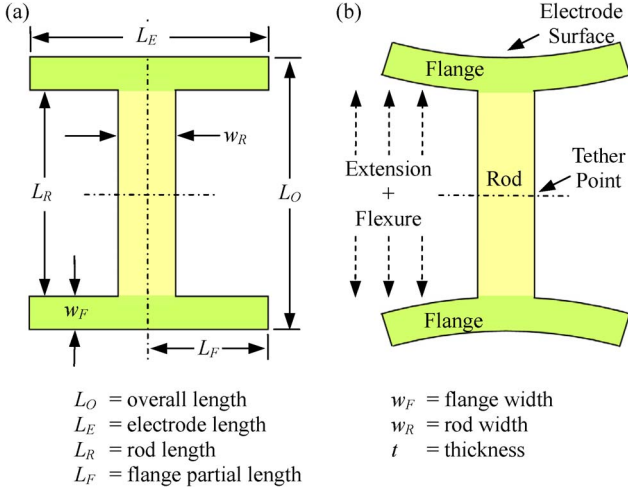
Fig. 3. IBAR design concept for high tunability and low motional resistance. (a) Undeformed geometry. (b) In the desired mode.

The IBAR is presented as the solution for temperature-compensated oscillators. The basic IBAR structure is a combination of two flexural flanges and an extensional rod [Fig. 3(a)]. The flanges provide large moving electrode area and low k_n/A_e for low R_1 and good electrostatic tuning. In the desired mode [Fig. 3(b)], the symmetric extensional nature of the rod minimizes anchor loss for high Q. Multi-section IBARs may be constructed by mechanically joining multiple rod and flange combinations. Multiple sections increase the transduction area and further reduce R_1. For example, the device shown in Fig. 1 is a two-section IBAR with two extended flanges.

The lumped model parameters for a resonator are found from the mode shapes. The dynamic mass can be found by integrating over the volume of the resonator V

$$m_n = \frac{2T_E}{\dot{u}_a^2} = \rho_m \frac{\int_V u^2(x,y,z)dV}{u_a^2} \quad (17)$$

in which T_E is the maximum kinetic energy, $\dot{u}_a$ is the time derivative of the displacement at a particular point of interest u_a, and $u(x,y,z)$ is the mode shape. Similarly

$$k_n = \frac{2V_E}{u_a^2} = \omega_n^2 m_n \quad (18)$$

in which V_E is the maximum elastic strain energy. A large displacement for a given V_E gives a small stiffness.

E. Generalized Capacitive Coupling

The coupling η for parallel-plate devices (10) is valid when the displacement of the entire electrode overlap area is uniform. It is desired to accommodate all resonators (i.e., including those with varying displacement along the electrode overlap area) using the same expression. The objective is to take the general mode shape and map it into a 1-D uniform parallel-plate equivalent with the same gap and electrode dimensions (Fig. 4). It can be shown that when u_a in (17) and (18) is the average
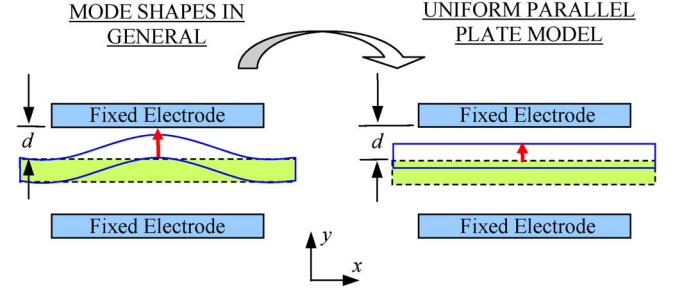

Fig. 4. Mapping of a general mode shape into a uniform 1-D parallel-plate equivalent. The dotted lines represent the unformed structure. The solid blue lines represent the mode shape.

TABLE I
MECHANICAL PROPERTIES OF SINGLE-CRYSTAL SILICON AT 298 K [29]

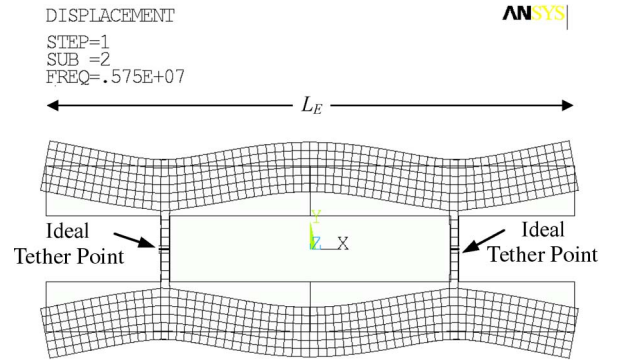|	Stiffness Coefficients [GPa] ±200ppm			Mass Density [kg/m³] ±100ppm
	C_{11}	C_{12}	C_{44}	ρ_m
Pure (ρ_e=10¹³)	165.64	63.94	79.51	2329.0
n-type (P, ρ_e=2×10¹⁹)	163.94	64.77	79.19	2329.7

Fig. 5. Mode shape of the two-section IBAR in Fig. 1, showing a symmetric mode shape and ideal anchoring locations.

displacement along the electrode overlap area, (10) holds true for all mode shapes.

Many modes exist for the IBAR structure. The desired mode is the only mode in which the displacements along the entire moving electrode surface are in phase. For the out-of-phase modes, the average displacement is reduced, leading to a larger k_n and, thus, larger R_1. For this reason, spurious modes are conveniently suppressed by capacitive coupling.

F. Finite-Element Modeling

Computational finite-element modeling is convenient for predicting natural frequencies and mode shapes from the geometry and material properties (Table I). ANSYS was utilized as the platform. In the analyses, the dynamic stiffness is computed numerically from ANSYS modal analysis results (see Fig. 5). Following (18), k_n is found from the strain energy in the desired mode and the associated average displacement along the electrode overlap area.

G. Comparison to Extensional-Mode Resonators

To evaluate the merits of the IBAR, we introduce the model of a pure extensional-mode (also known as longitudinal-mode) resonator for comparison. Pure extensional modes have been found in plate-like silicon bulk acoustic resonators [5]. The angular natural frequencies of a 1-D extensional-mode resonator are given by

$$\omega_n = \frac{n\pi\, v_a}{L} \tag{19}$$

in which n is the mode number and L is the frequency-defining length. The dynamic mass and stiffness at one of the ends are, respectively [4]

$$m_{n,\text{1D-ext}} = \frac{\rho_m L A_e}{2} \tag{20}$$

$$k_{n,\text{1D-ext}} = \frac{n^2\pi^2 E_i A_e}{2L}. \tag{21}$$

The normalized dynamic stiffness can be expressed as a direct function of natural frequency

$$\left(\frac{k_n}{A_e}\right)_{\text{1D-ext}} = n\pi^2 \sqrt{E_i\rho_m} \cdot f_n. \tag{22}$$

Assuming that $E_i = 168$ GPa for a resonator aligned to $\langle 110 \rangle$, the k_n/A_e for the fundamental extensional mode is 0.195 PN $\cdot$ m^{-3} $\cdot$ MHz^{-1} (1 PN $= 1 \times 10^{15}$ N).

To conveniently compare an IBAR to a 1-D extensional-mode resonator, the relative dynamic compliance c_r and relative dynamic stiffness k_r are defined

$$c_r \equiv \frac{1}{k_r} \equiv \frac{\left(\frac{k_n}{A_e}\right)_{\text{1D-ext},f_n}}{\left(\frac{k_n}{A_e}\right)_{\text{IBAR},f_n}}. \tag{23}$$

c_r is the ratio of normalized dynamic stiffness of two resonators at the same frequency. An IBAR will have a factor of c_r improvement in tuning over an extensional-mode resonator at the same frequency.

IBARs can be classified into three categories: compliance-enhanced (CE), Q-enhanced, and semicompliant high-Q [30]. CE IBARs have substantial response in the flange and minimal displacement of the rod. They have the lowest k_n/A_e and provide the greatest tunability. In CE IBARs, the natural frequency of the desired mode is primarily defined by the flange [30]. Plots of c_r generated from finite-element analysis data permit easy evaluation of CE IBARs. In Fig. 6, the c_r's of IBARs with flange widths of 5, 10, 20, and 40 μm are plotted versus frequency. Since flange flexing (i.e., beam bending) is dominant in the mode for CE IBARs, the compliance is inversely proportional to the flange width. A 1-MHz IBAR with $w_F = 40$ μm can have a maximum c_r of 17. For $w_F = 10$ μm, the maximum c_r at 1 MHz is 68. The empirical formula for the maximum relative dynamic compliance of an IBAR is given by

$$c_r \equiv c_{r,\text{1MHz}} \cdot \left(\frac{f_n}{1\,\text{MHz}}\right)^{-1} \tag{24}$$

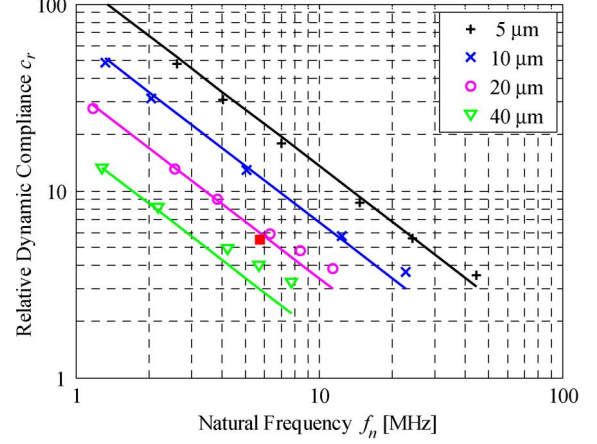
Fig. 6. Relative dynamic compliance limit of IBARs with $w_F = [5, 10, 20, 40]$ μm and two fixed electrodes to extensional-mode resonators. Markers represent finite-element analysis data. Lines represent (24). The red square marker represents the 6-MHz two-section IBAR in Fig. 1.

TABLE II
MAXIMUM RELATIVE DYNAMIC COMPLIANCE OF A CE IBAR
AT 1 MHz FOR THE EMPIRICAL FORMULA IN (24)

w_E [μm]	Maximum $c_{r,\text{1MHz}}$
5	136
10	68
20	34
40	17

where $c_{r,\text{1MHz}}$'s for several values of w_F are listed in Table II. For $w_F = 10$ μm, c_r is estimated to be 2.3 at 30 MHz. At higher frequencies, c_r is further reduced, and the tuning characteristics of an IBAR become more similar to that of an extensional-mode resonator.

H. Figure of Merit

Resonators configured with device capacitances shunted to a common node (Fig. 2) have a figure of merit

$$F_{M,S} \equiv (R_1 \cdot 2\pi f_s C_S)^{-1} \tag{25}$$

which relates the susceptance through the shunt capacitance C_S to the admittance of the motional arm at resonance. Substituting for R_1 and C_S

$$F_{M,S} \approx -Q_U \gamma_e V_{Pi}^2. \tag{26}$$

The figure of merit is linearly dependent on the electrostatic tuning coefficient γ_e and V_{Pi}^2.

III. FABRICATION

IBARs with center frequencies from 1 to 30 MHz have been fabricated using the high-aspect-ratio-polysilicon-and-single-crystal-silicon (HARPSS)-on-silicon-on-insulator (SOI) process [5]. The process flow in Fig. 7 requires three masks. The process starts with thermally growing a 0.5–1.5-μm-thick oxide layer on a low-resistivity SOI substrate. The oxide is patterned, retaining only the regions defining the resonator structure and anchors [Fig. 7(a)]. Vertical trenches are then
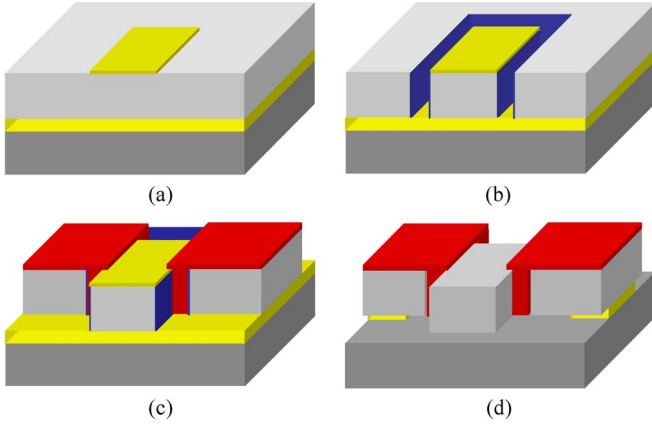
Fig. 7. The three-mask HARPSS-on-SOI process for fabrication of thick SCS resonators with submicrometer gaps. After [5]. (a) Grow and pattern initial oxide. (b) Etch trenches to define the structure. Deposit sacrificial oxide and etch-back oxide in the field. (c) Deposit LPCVD polysilicon. Pattern and etch field and polysilicon to define the pads and fixed electrodes. (d) Release structures in HF. The SCS resonator is suspended and separated from the polysilicon fixed electrodes.
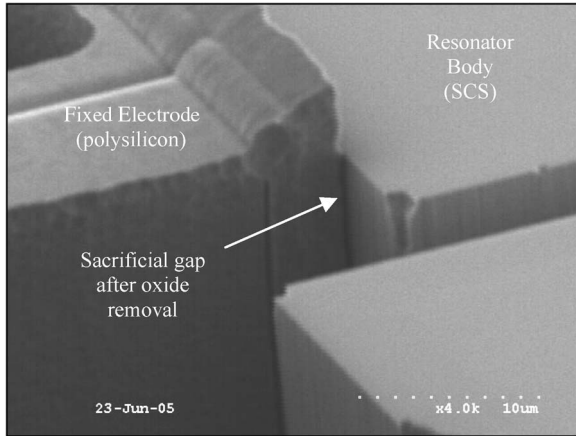

Fig. 8. SEM of a 180-nm gap created in the HARPSS-on-SOI process.

created using deep reactive-ion etching through the device layer. The thickness of the resonators can be greater than 50 μm. A thin conformal layer of sacrificial oxide is disposed by either low-pressure chemical vapor deposition (LPCVD) or thermal oxidation. The thickness of the sacrificial oxide layer determines the capacitive gap between the SCS resonator and soon-to-be trench-refilled fixed electrodes. Typical gap sizes are 60–500 nm. The sacrificial oxide is then etched back on the surface [Fig. 7(b)]. Next, highly-doped p-type LPCVD polysilicon fills the trenches and forms the fixed electrodes. Polysilicon is also deposited directly on the exposed silicon to anchor the fixed electrodes. Next, the input/output pads and polysilicon fixed electrodes are patterned and etched to provide electrical isolation between the pads and the resonator body [Fig. 7(c)]. Structures are finally released in hydrofluoric acid [Fig. 7(d)]. Fig. 1 shows a scanning electron micrograph (SEM) of a 10-μm-thick IBAR with conservative 180-nm gaps. The gap size was chosen to suit the design operational voltage range of 15–25 V. The close-up of the gap (Fig. 8) shows uniformity along the thickness of the device.

TABLE III
6-MHz IBAR SUMMARY

	Model	Measured
Center Frequency	5.75 MHz	5.59 MHz
Unloaded Q, Q_U	-	112000
Norm. Dyn. Stiffness, k_n/A_e	0.204 PN/m^3	-
Rel. Dyn. Compliance, c_r	5.50	-
Overall Length, L_O	100 μm	
Electrode Length, L_E	320 μm	
Flange Width, w_F	30 μm	
Rod Length, L_R	40 μm	
Rod Width, w_R	5 μm	
Thickness, t	10 μm	
For gap d = 180 nm		
- R_1*, V_P= 3 V	53 kΩ	58 kΩ
- R_1*, V_P= 10 V	2.6 kΩ	10.7 kΩ
- R_1*, V_P= 20 V	0.6 kΩ	6.8 kΩ
- C_1, V_P= 3 V	4.7 aF	-
- C_1, V_P= 20 V	422 aF	-
- $F_{M,S}$, V_P= 3 V	3.33	-
- $F_{M,S}$, V_P= 20 V	301	-
- Tuning coefficient, γ_e	-7.44 ppm/V^2	-7.92 ppm/V^2
For gap d = 65 nm		
- R_1, V_P= 3 V	0.90 kΩ	-
- $F_{M,S}$, V_P= 3 V	96	
- Tuning coefficient, γ_e	-158 ppm/V^2	-

* Theoretical R_1, C_1, and $F_{M,S}$ are calculated assuming V_{Bi} =1V and Q_U=112000.

IV. RESONATOR MEASUREMENTS AND ANALYSIS

Characterization of the fabricated resonators was performed with direct connection to an Agilent 4395A network analyzer with a resistive divider test set [4]. Resonators were wire-bonded to a PCB and placed inside a custom vacuum chamber. The measured transmission characteristic is the voltage ratio A_V.[6] From the measured transmission, the test resistance R_t is given by

$$R_t = 50 \ \Omega \cdot \left(10^{\frac{-A'_V}{20}} - 1\right) \qquad (27)$$

where A'_V is the voltage ratio at resonance. The device parameters can then be extracted from R_t, the center frequency, and the measured quality factor.

For the IBAR in Fig. 1, the predicted frequency is 5.75 MHz (Table III). Finite-element data give a k_n/A_e of 0.204 PN/m^3. From this, c_r is 5.50, and the predicted tuning coefficient is -7.44 ppm/V^2.

A Q_L of 10 3000 was measured in vacuum with a polarization voltage V_P of 3 V (Fig. 9). The bias potential of the fixed electrodes $V_{B1} = V_{B2}$ was 1 V. The measured center frequency is 5.59 MHz.[7] Changes in quality factor were not observable over the pressure range of 0.1 torr–1 μtorr. Flexural beam

---

[6]A_V is not equal to s_{21}.

[7]The measured center frequency is the resonant frequency of the device f_r with shunt and parallel capacitances in effect. For the disclosed IBARs and experimental configuration, the measured f_r in this paper can be considered equal to the resonant frequency of the motional arm f_s.
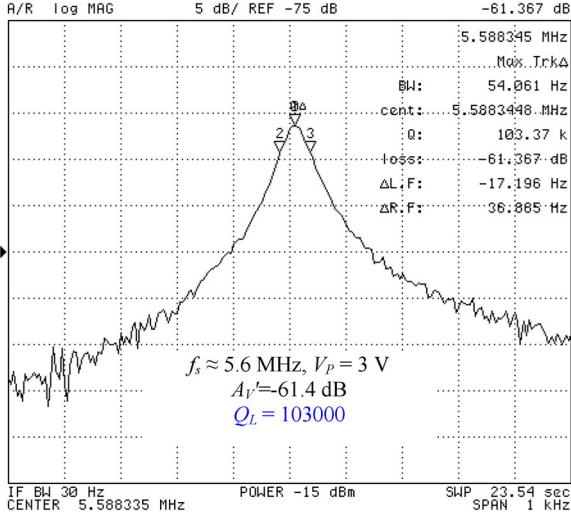
Fig. 9. Measured frequency response of the 6-MHz two-section IBAR with $V_P = 3$ V, $V_{Bi} = 1$ V, and $P = 0.1$ torr.
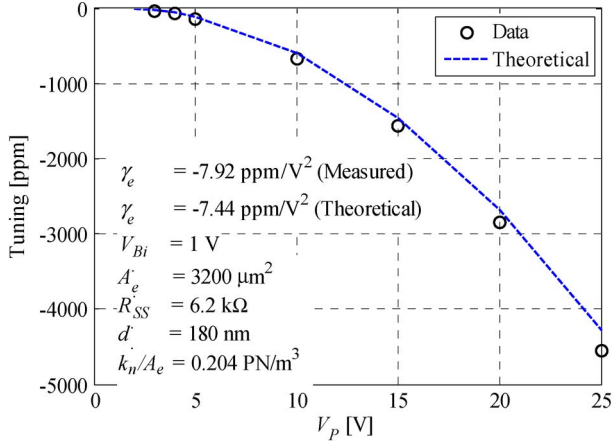

Fig. 10. Measured and theoretical tuning characteristics of the 6-MHz IBAR over a V_P range of 2–25 V.
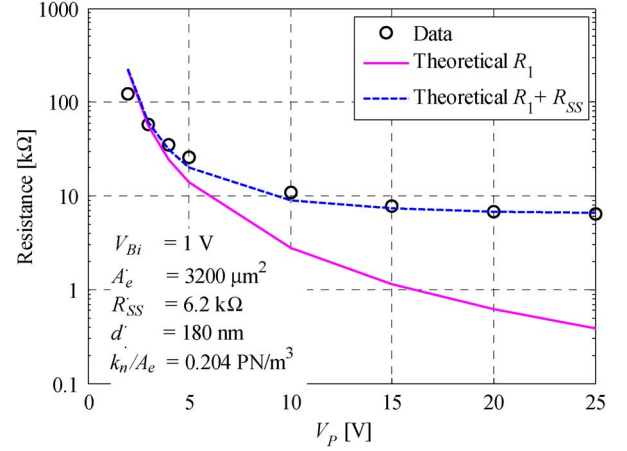

Fig. 11. Measured and theoretical resistances of the 6-MHz IBAR over a V_P range of 2 to 25 V. The dotted line represents the predicted resistance accounting for R_{SS} of 6.2 kΩ.
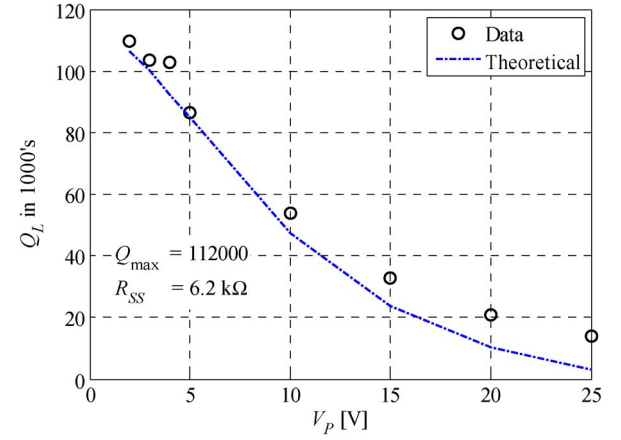

Fig. 12. Measured and theoretical loaded Q's of the 6-MHz IBAR over a V_P range of 2–25 V.

resonators near 1 MHz are typically limited by thermoelastic damping (TED) [31], [32]. Assuming pure flexure in the IBAR with a 30-μm-wide flange, the peak TED frequency is approximately 100 kHz, and the limiting Q at 5.5 MHz is 350 000. Therefore, this IBAR is not Q-limited by TED. The measured Q is possibly limited by asymmetries in the lithography and etching that lead to anchor loss.

The measured electrostatic tuning and resistance of the IBAR are as expected. By tuning V_P from 2 to 25 V with V_{Bi} set at 1 V, f_s is tuned by 4557 ppm (Fig. 10). The measured electrostatic tuning coefficient for this device is -7.92 ppm/V^2. The test resistance R_t is 6.8 kΩ with V_P of 20 V, while the predicted motional resistance R_1 is 0.6 kΩ (Fig. 11). A large part of R_t is a small-signal resistance R_{SS} of approximately 6.2 kΩ. R_{SS}'s of 0.5–5 kΩ have been measured in other IBARs (Fig. 23). It is a result of the finite conductance of the resonator body. Since most capacitive resonators reported to date have R_1 larger than several k-Ω, R_{SS} and its affects have not been observed in the past. In IBARs, R_{SS} can substantially reduce

Q_L as R_1 is reduced (Fig. 12). The loaded Q can be expressed as

$$Q_L = Q_U \frac{R_1}{R_1 + R_{SS} + R_{term}} \quad (28)$$

where R_{term} is the sum of the termination impedances. Dependence of Q_L on V_P is also observed in other IBARs (Fig. 24). It would be beneficial to reduce the loading for low close-to-carrier phase noise. However, since the stabilized $R_1 + R_{SS}$ over the voltage range is advantageous for interfacing, eliminating R_{SS} is neither necessary nor desirable.

V. OSCILLATOR DESIGN AND CHARACTERIZATION

An oscillator (Fig. 2) based on the IBAR was implemented to demonstrate a temperature-stable reference. Table IV is a summary of the two-chip solution with an overall frequency stability of 39 ppm over 100 °C. The compensation scheme and the measured temperature dependence of frequency are presented. The interface circuit was fabricated in a two-poly three-metal 0.5-μm CMOS process through AMI Semiconductor. The die photograph is shown in Fig. 13. The design of the

| Circuit Specifications	
Amplifier GBW product	175 MHz
Charge pump clock	1 MHz
Ripple filter -3dB freq.	1 kHz
Total power consumption w/ linear compensation w/ parabolic compensation	1.8 mW 1.9 mW
Die area (for either IC)	2.25 mm^2
Oscillator Specifications	
Freq. stability over 100°C Uncompensated w/ linear compensation w/ parabolic compensation	2830 ppm 334 ppm **39 ppm**
Phase Noise performance f_m = 10 Hz f_m = 1 kHz Noise floor, f_m >10 kHz	-66 dBc/Hz -112 dBc/Hz -135 dBc/Hz
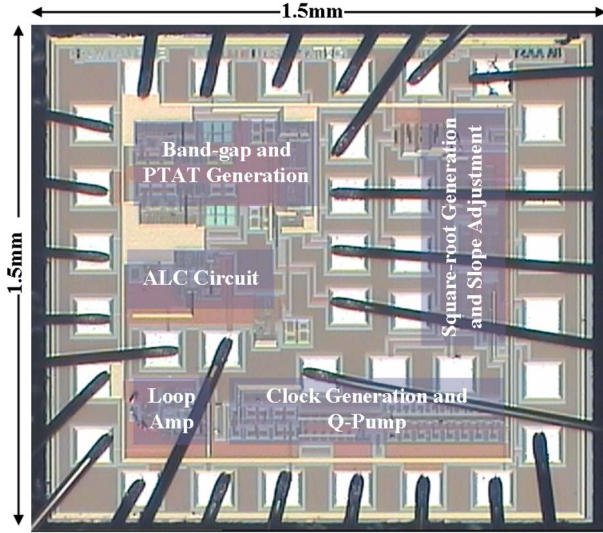
Fig. 13. Die photograph of the interface IC with ALC loop amplifier and parabolic TC circuitry.

circuit is documented in detail in [17]. The power consumption for sustaining oscillations and TC was 1.9 mW.

A. Temperature Compensation

The oscillator center frequency is nominally equal to the resonant frequency of the motional arm of the resonator

$$f_s(V_{Pi}, T) = f_n(T) + \Delta f_e(V_{Pi}). \qquad (29)$$

The objective is to stabilize f_s by negating the shift in f_n by tuning Δf_e. Substituting for Δf_e

$$f_s(V_{Pi}, T) = f_n(T) \left[1 + \gamma_e \cdot V_{Pi}(T)^2 \right]. \qquad (30)$$

Assuming that f_n has a linear dependence on T, (30) can be rearranged to solve for V_{Pi}^2 under the condition that f_s is held constant

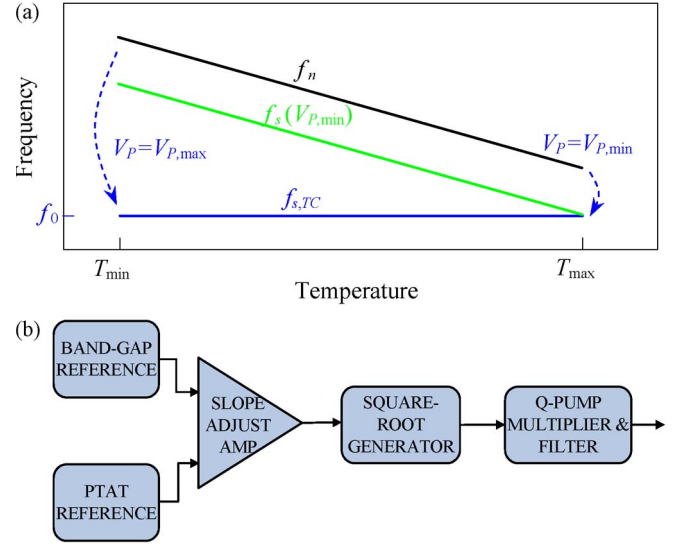$$V_{Pi}^2 \approx A - B \cdot \Delta T. \qquad (31)$$

Fig. 14. (a) Illustrated mechanics of TC by V_P-correction and (b) parabolic TC circuit (bias generator).

A is used for setting the center frequency f_0, and B is approximated by

$$B \cong \frac{\gamma_T}{\gamma_e} \qquad (32)$$

in which both γ_T and γ_e are negative values. The illustrated mechanics of TC and the block diagram for the compensation circuit are shown in Fig. 14.

B. Interface IC Design

The interface IC consists of a transimpedance amplifier to sustain oscillations and an automatic level control (ALC) circuit to control the power input to the resonator (see Fig. 2). Level control is accomplished by detecting the amplitude of oscillations, comparing it to a reference voltage V_{REF}, and using the difference to control the gain of a feedback MOS resistor R_{AMP}. The reference voltage used for comparison is dependent on the drive-level linearity of the resonator. The ALC circuit is able to accommodate the resistance variation over the V_P-tuning range since R_{SS} stabilizes the resonator resistance.

The TC circuit (Fig. 14) comprises band-gap and proportional-to-absolute-temperature (PTAT) voltage generators that feed low-power scaling and difference amplifiers. The coefficients A and B of (31) are adjustable using different gain-setting resistors in the amplifiers to accommodate the tuning coefficients of different resonators.

Since the V_P-tuning characteristic is parabolic, a square-root generator is required for accurate TC. This function is provided by the simple square-law relation between the drain current and the V_{GS} of a MOS transistor biased above V_T. The last stage of the difference amplifier is designed to be a transconductance stage that feeds a PTAT current into a square-rooting circuit. The square-rooting circuit generates a voltage proportional to the square root of the current, thus providing the required temperature coefficient.
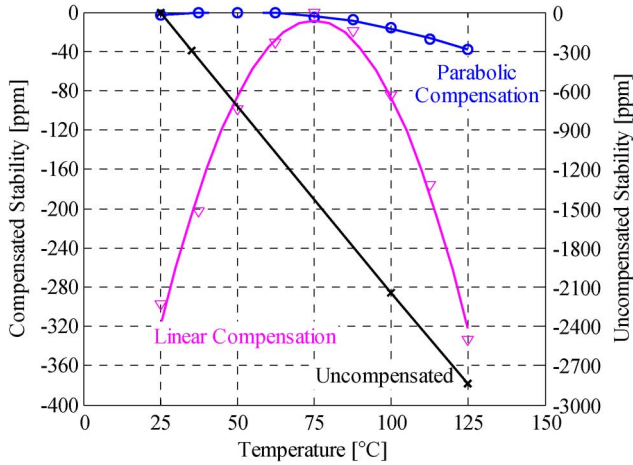
Fig. 15. Uncompensated, linearly compensated, and parabolically compensated temperature stability for a 6-MHz IBAR oscillator measured over a range of 100 °C. Stability improved 72 times with parabolic compensation.

Fig. 16. Measured single-sideband phase noise of the 6-MHz IBAR oscillator.

A charge-pump voltage multiplier steps up the generated voltage to a maximum of 25 V. A Dickson-type charge pump [33] was selected in this implementation to obviate the need for high-voltage transistors. The change in the temperature slope arising from the charge-pump diodes is also accounted for while choosing the gain-setting resistors for the PTAT amplifier.

C. Temperature Stability

The 6-MHz oscillator exhibited a temperature variation of only 39 ppm over 100 °C with parabolic TC (Fig. 15)—an improvement factor of 72 over the uncompensated variation. See Table IV. Thermal equilibrium was ensured in the temperature chamber before measurements were taken. It is estimated that the curvature of the band-gap and PTAT generators account for almost 25 ppm in error and can be minimized with curvature correction techniques. Other errors include the nonlinearity in the square-root generator, the temperature coefficient mismatch in the charge-pump diodes, and inaccuracies in setting B.

D. Phase Noise

The phase noise of the IBAR oscillator (Fig. 16) is presented to show oscillator functionality and close-to-carrier noise. Aside from the ALC circuitry, there were no attempts at minimizing phase noise. Measurements were made with an Agilent E5500 phase noise analyzer. The IBAR was biased at 3 V to investigate the close-to-carrier noise. A low V_P was used because Q is minimally loaded with this condition. The phase noise is -90 dBc/Hz at 100-Hz offset and -110 dBc/Hz at 1-kHz offset. The far-from-carrier phase noise of the oscillator with ALC was -135 dBc/Hz. The effects of V_P noise and resonator linearity have not been thoroughly studied. It is possible that these effects contribute to the unexpected $1/f_m^2$ noise. In systems that contain a PLL synthesizer for upconversion, the noise floor is further suppressed. In such applications, resonator Q has more significance than linearity. Nonetheless, methods to reduce Q loading and further improve resonator linearity are proposed hereinafter.
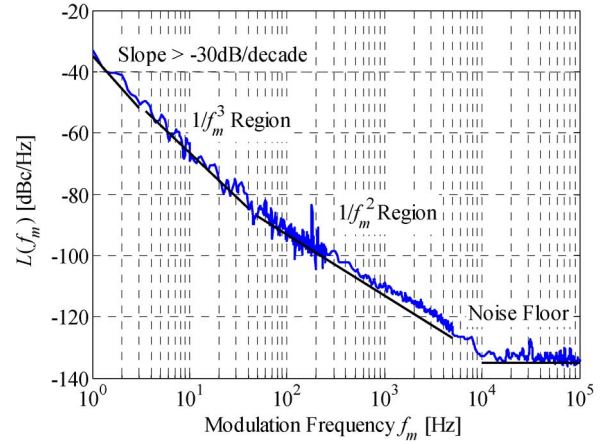
VI. FURTHER DISCUSSION

The successful implementation of a temperature-stable reference oscillator provides an excellent benchmark for further improvement. Achieving center-frequency accuracy [30] is one major step toward manufacturability. A thorough study on the phase noise is necessary. Also, several aspects of the resonator can be improved.

A. IBAR Improvements

Desirable improvements to the IBAR include lower operational voltage, greater tunability, improved linearity, and optimizing R_{SS}. To accomplish this, smaller capacitive gaps, a thicker substrate, and fixed electrodes on the inner surfaces of the flange will be beneficial.

Smaller 65-nm gaps were fabricated for a 20-MHz IBAR (Fig. 17). Due to the smaller gaps, this higher frequency device has sufficient tuning range and low R_1 for voltages not exceeding 15 V (Fig. 18). If the gaps of the 6-MHz IBAR are reduced to 65 nm, R_1 is 0.90 kΩ for 3-V polarization (see Table III). At the same time, γ_e will be magnified by a factor of 21 to -158 ppm/V^2. For such a device, a V_{Pi} range of 3–6 V provides $\sim$4300 ppm of tuning.

A thicker substrate will improve linearity and reduce R_1 and R_{SS} (Fig. 20). The increase in electrode overlap area by extending thickness is desirable in all performance aspects. Mode shapes in IBARs are generally planar and have negligible dependence on thickness when t is a quarter wavelength or less.

Inner surface electrodes are expected to provide a significant improvement. R_{SS} will be reduced because charge will migrate only across the width of the flange in each half cycle. Additionally, since electrode area can be almost doubled, R_1 can be reduced by a factor of approximately four. Most importantly, lower polarization voltages (and greater drive-level linearity) are possible since γ_e and c_r will be doubled.

B. Compensation Accuracy

As the temperature is sensed on the IC, dynamic thermal gradients between the two chips limit the accuracy of compensation. An optimal packaging solution would ensure minimal
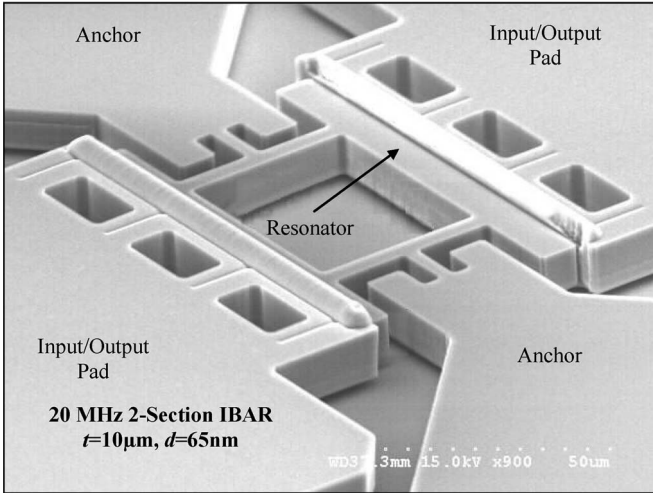
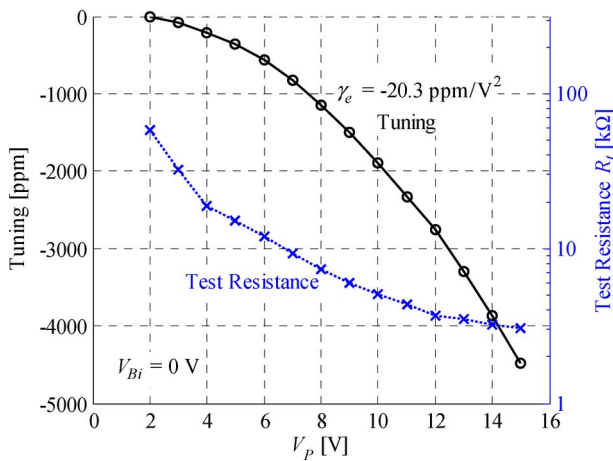Fig. 17.   SEM of a 20-MHz 10-μm-thick two-section 65-nm-gap IBAR.

Fig. 18.   Measured tuning and resistance of the 20-MHz IBAR with 65-nm gaps ($V_{B1} = V_{B2} = 0$ V).

thermal resistance between the resonator and the PTAT generator. Compensation accuracy is also limited by error sources from the IC [17].

C. Applications

The achieved temperature stability and current consumption satisfy the requirements for medium-performance oscillators. The measured stability is superior to ceramic and CMOS counterparts [34], [35]. Although significant advancements are necessary to reach TCXO-grade performance, there are a number of immediate applications for this technology. One ideal application is a small-form-factor consumer-grade timing reference. In applications in which tracking is desired, V_P-tuning also offers dynamic control.

VII. CONCLUSION

A low-power temperature-compensated oscillator with 39-ppm stability over a range of 100 °C, based on a new micromechanical capacitive resonator and a new compensation architecture, has been achieved. Oscillator measurements confirm
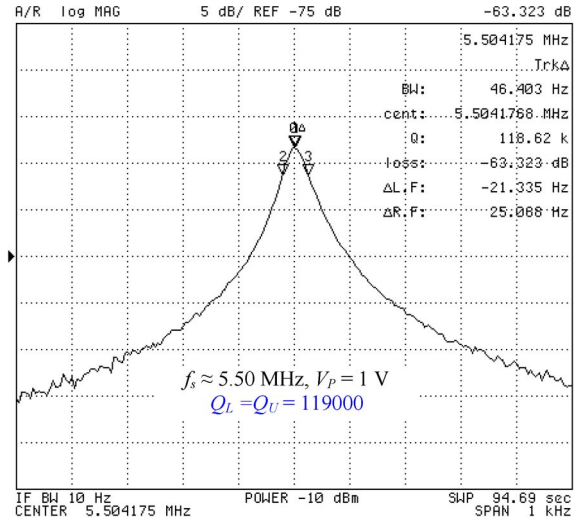

Fig. 19.   Measured Q of 119 000 from a 6-MHz three-section IBAR in vacuum ($V_P = 1$ V, $V_{Bi} = 0$ V).

that the described technology is attractive over alternatives for medium-performance timing in the 1–30-MHz spectrum. The automatic compensation technique involves electrical tuning of the resonant frequency. Several implementations of the unique resonator topology have been characterized and verified to have high tunability, high Q, and low motional resistance. The experimental results confirm that the design objectives have been met. Quality factors exceeding 100 000 have been measured. A modest amount of electrical tuning, sufficient for TC, has been demonstrated. Motional resistances have been reduced to the extent that a small-signal resistance in the resonators has been observed. This unexpected resistance is beneficial for stabilizing the resonator impedance over the tuning range.

Improvements are suggested for future work. Reducing the small-signal resistance loading will ensure high Q throughout the tuning range. The measured phase noise serves as a baseline for further improvement. Incorporating additional electrodes is expected to reduce both resistive loading and phase noise. The accuracy of TC can also be improved.

One objective of this paper is to lay a practical foundation. The described resonator circumvents the typical high voltages associated with capacitive micromechanical devices. Manufacturability and initial frequency accuracy are presented in [30]. Only time will tell which applications will benefit most from this unique resonator and oscillator architecture.

APPENDIX

The experimental results from a 20-μm-thick three-section 6-MHz IBAR are presented. The open-loop response with $V_P = 1$ V and $V_B = 0$ V shows an unloaded Q of 119 000 (Fig. 19). The test resistance when $V_P = 18$ V is 655 Ω (Fig. 20), of which 437 Ω is attributed to the resistive loading of the resonator body, fixed electrodes, and electrical terminations. The de-embedded motional resistance is therefore only 218 Ω. The low R_1 is a result of increased electrode length and increased thickness. The tuning and test resistance of the resonator are shown in Fig. 21.
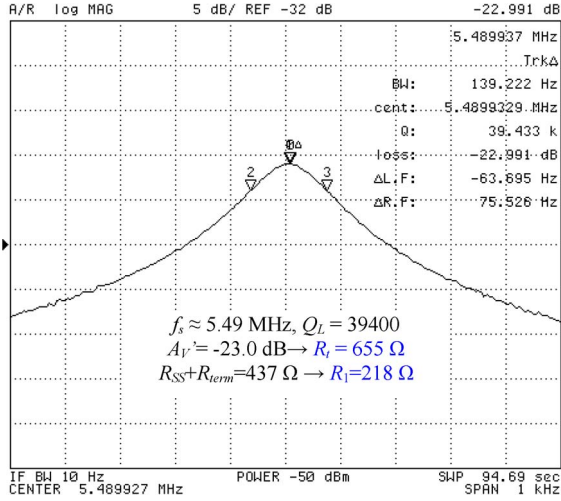
Fig. 20. Lowest measured resistance of 655 Ω ($R_1 = 218$ Ω) from the 6-MHz three-section IBAR ($V_P = 18$ V, $V_{Bi} = 0$ V).
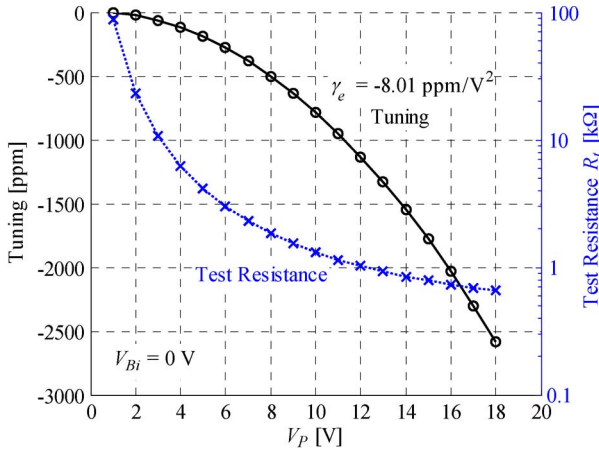

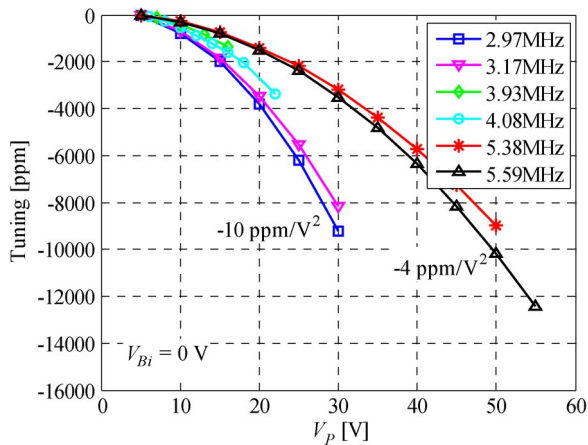Fig. 21. Measured tuning and resistance of the 6-MHz three-section IBAR with 180-nm gaps.

Fig. 22. Measured tuning characteristics of several 3–6 MHz IBARs with 270-nm gaps.

The tuning, test resistance, and loaded Q for other IBARs have been measured over a range of V_P. Characteristics similar to that of the two- and three-section 6-MHz IBARs are observed. The reported data in Figs. 22–24 are from the same
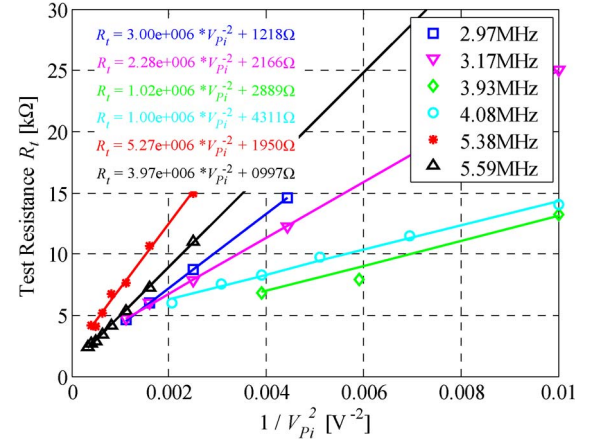

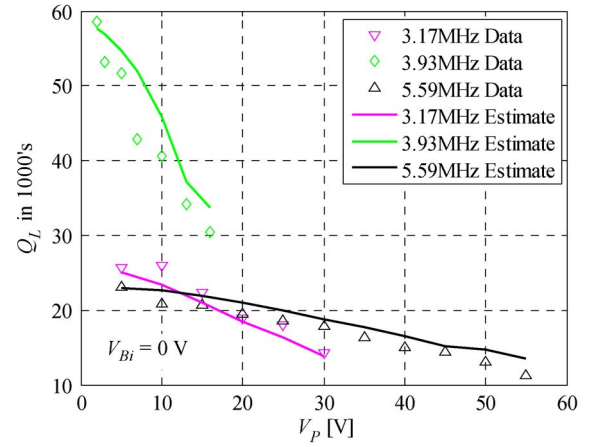Fig. 23. Measured test resistance dependence on V_{Pi} for several 3–6-MHz IBARs with 270-nm gaps.

Fig. 24. Quality factor loading in several 3–6-MHz IBARs with 270-nm gaps.

10-μm substrate with 270-nm gaps. From Fig. 22, the 3-MHz devices clearly have greater tuning than the 5-MHz devices. A linear fit is applied to the measured test resistances in Fig. 23. A constant resistance of 1–5 kΩ is observed in R_t, signifying the presence of R_{SS}. Finally, the loaded-Q characteristic in Fig. 24 shows once again the presence of R_{SS} in low-resistance resonators.

REFERENCES

[1] C. T.-C. Nguyen, "MEMS technology for timing and frequency control," *IEEE Trans. Ultrason., Ferroelectr., Freq. Control*, vol. 54, no. 2, pp. 251–270, Feb. 2007.
[2] K. M. Lakin, "Thin film resonator technology," *IEEE Trans. Ultrason., Ferroelectr, Freq. Control*, vol. 52, no. 5, pp. 707–716, May 2005.
[3] G. Piazza, P. H. Stephanou, and A. P. Pisano, "Piezoelectric aluminum nitride vibrating contour-mode MEMS resonators," *J. Microelectromech. Syst.*, vol. 15, no. 6, pp. 1406–1418, Dec. 2006.
[4] G. K. Ho, R. Abdolvand, A. Sivapurapu, S. Humad, and F. Ayazi, "Piezoelectric-on-silicon lateral bulk acoustic wave micromechanical resonators," *J. Microelectromech. Syst.*, vol. 17, no. 2, pp. 512–520, Apr. 2008.

[5] S. Pourkamali, G. K. Ho, and F. Ayazi, "Low-impedance VHF and UHF capacitive silicon bulk acoustic wave resonators—Part I: Concept and fabrication," *IEEE Trans. Electron Devices*, vol. 54, no. 8, pp. 2017–2023, Aug. 2007.

[6] H. J. McSkimin, "Measurement of elastic constants at low temperature by means of ultrasonic waves data for silicon and germanium single crystals and for fused silica," *J. Appl. Phys.*, vol. 24, no. 8, pp. 988–997, Aug. 1953.

[7] W. T. Hsu and C. T.-C. Nguyen, "Geometric stress compensation for enhanced thermal stability in micromechanical resonators," in *Proc. IEEE Ultrason. Symp.*, Sendia, Japan, Oct. 5–8, 1998, pp. 945–948.

[8] W.-T. Hsu, J. R. Clark, and C. T.-C. Nguyen, "Mechanically temperature-compensated flexural-mode micro-mechanical resonators," in *IEDM Tech. Dig.*, Dec. 2000, pp. 399–402.

[9] K. M. Lakin, K. T. McCarron, J. F. McDonald, and J. Belsick, "Temperature coefficient and ageing in BAW composite materials," in *Proc. IEEE Int. Freq. Control Symp.*, Seattle, WA, Jun. 2001, pp. 605–608.

[10] R. Abdolvand, G. K. Ho, and F. Ayazi, "ZnO-on-nanocrystalline diamond lateral bulk acoustic resonators," in *Proc. IEEE MEMS Conf.*, Kobe, Japan, Jan. 2007, pp. 795–798.

[11] B. Kim, R. Melamud, M. A. Hopcroft, S. A. Chandorkar, G. Bahl, M. Messana, R. N. Candler, G. Yama, and T. Kenny, "Si–SiO2 composite MEMS resonators in CMOS compatible wafer-scale thin-film encapsulation," in *Proc. IEEE Int. Freq. Control Symp.*, Geneva, Switzerland, May 2007, pp. 1214–1219.

[12] W.-T. Hsu, A. R. Brown, and K. R. Cioffi, "A programmable MEMS FSK transmitter," in *Proc. IEEE ISSCC*, San Francisco, CA, Feb. 6–9, 2006, pp. 1111–1120.

[13] M. Lutz, A. Partridge, P. Gupta, N. Buchan, E. Klaassen, J. McDonald, and K. Petersen, "MEMS oscillators for high volume commercial applications," in *Tech. Dig. 14th Int. Conf. Solid-State Sens., Actuators, Microsyst. (Transducers)*, Lyon, France, Jun. 10–14, 2007, pp. 49–52.

[14] K. Sundaresan, G. K. Ho, S. Pourkamali, and F. Ayazi, "A low phase noise 100 MHz silicon BAW reference oscillator," in *Proc. IEEE CICC*, San Jose, CA, Sep. 10–13, 2006, pp. 841–844.

[15] M. Hopcroft, R. Melamud, R. N. Candler, W.-T. Parl, B. Kim, G. Yama, A. Partridge, and T. W. Kenny, "Active temperature compensation for micromachined resonators," in *Tech. Dig. Solid-State Sens., Actuator Microsyst. Workshop*, Hilton Head Island, SC, Jun. 2004, pp. 364–367.

[16] G. K. Ho, F. Ayazi, S. Pourkamali, and K. Sundaresan, "Highly tunable low-impedance capacitive micromechanical resonators, oscillators, and processes relating thereto," U.S. Patent 7 511 870, Mar. 31, 2009.

[17] K. Sundaresan, G. K. Ho, S. Pourkamali, and F. Ayazi, "Electronically temperature compensated silicon bulk acoustic resonator reference oscillators," *IEEE J. Solid-State Circuits*, vol. 42, no. 6, pp. 1425–1434, Jun. 2007.

[18] M. E. Frerking, *Crystal Oscillator Design and Temperature Compensation*. New York: Van Nostrand Reinhold, 1978, p. 27.

[19] T. H. Lee and A. Hajimiri, "Oscillator phase noise: A tutorial," *IEEE J. Solid-State Circuits*, vol. 35, no. 3, pp. 326–336, Mar. 2000.

[20] E. Rubiola and V. Giordano, "On the $1/f$ frequency noise in ultra-stable quartz oscillators," *IEEE Trans. Ultrason., Ferroelectr., Freq. Control*, vol. 54, no. 1, pp. 15–22, Jan. 2007.

[21] W. C. Tang, T.-C. H. Nguyen, and R. T. Howe, "Laterally driven polysilicon resonant microstructures," in *Proc. IEEE MEMS Conf.*, Feb. 20–22, 1989, pp. 53–59.

[22] C. T.-C. Nguyen and R. T. Howe, "An integrated CMOS micromechanical resonator high-Q oscillator," *IEEE J. Solid-State Circuits*, vol. 34, no. 4, pp. 440–455, Apr. 1999.

[23] K. Wang, A.-C. Wong, and C. T.-C. Nguyen, "VHF free-free beam high-Q micromechanical resonators," *J. Microelectromech. Syst.*, vol. 9, no. 3, pp. 347–360, Sep. 2000.

[24] S. Pourkamali, A. Hashimura, R. Abdolvand, G. K. Ho, A. Erbil, and F. Ayazi, "High-Q single crystal silicon HARPSS capacitive beam resonators with self-aligned sub-100 nm transduction gaps," *J. Microelectromech. Syst.*, vol. 12, no. 4, pp. 487–496, Aug. 2003.

[25] S. Pourkamali, Z. Hao, and F. Ayazi, "VHF single crystal silicon elliptic bulk-mode capacitive disk resonators—Part II: Implementation and characterization," *J. Microelectromech. Syst.*, vol. 13, no. 6, pp. 1054–1062, Dec. 2004.

[26] J. R. Clark, W.-T. Hsu, M. A. Abdelmoneum, and C. T.-C. Nguyen, "High-Q UHF micromechanical radial-contour mode disk resonators," *J. Microelectromech. Syst.*, vol. 14, no. 6, pp. 1298–1310, Dec. 2005.

[27] Y. Jimbo and K. Itao, "Energy loss of a cantilever vibrator," *J. Horolog. Inst. Jpn.*, vol. 47, pp. 1–15, 1968.

[28] Z. Hao, A. Erbil, and F. Ayazi, "An analytical model for support loss in micromachined beam resonators with in-plane flexural vibrations," *Sens. Actuators A, Phys.*, vol. 109, no. 1/2, pp. 156–164, Dec. 2003.

[29] J. J. Hall, "Electronic effects in the elastic constants of n-type silicon," *Phys. Rev.*, vol. 161, no. 3, pp. 756–761, Sep. 1967.

[30] G. K. Ho, J. K.-C. Perng, and F. Ayazi, "Micromechanical IBARs: Modeling and process compensation," *J. Microelectromech. Syst.*, vol. 19, no. 3, Jun. 2010.

[31] B. Kim, M. A. Hopcroft, R. N. Candler, C. M. Jha, M. Agarwal, R. Melamud, S. A. Chandorkar, G. Yama, and T. W. Kenny, "Temperature dependence of quality factor in MEMS resonators," *J. Microelectromech. Syst.*, vol. 17, no. 3, pp. 755–766, Jun. 2008.

[32] R. Abdolvand, H. Johari, G. K. Ho, A. Erbil, and F. Ayazi, "Quality factor in trench-refilled polysilicon beam resonators," *J. Microelectromech. Syst.*, vol. 15, no. 3, pp. 471–478, Jun. 2006.

[33] J. Dickson, "On-chip high-voltage generation in MNOS integrated circuits using an improved voltage multiplier technique," *IEEE J. Solid-State Circuits*, vol. SSC-11, no. 3, pp. 374–378, Jun. 1976.

[34] K. Sundaresan, P. E. Allen, and F. Ayazi, "Process and temperature compensation in a 7-MHz CMOS clock oscillator," *IEEE J. Solid-State Circuits*, vol. 41, no. 2, pp. 433–442, Feb. 2006.

[35] M. S. McCorquodale, S. M. Pernia, J. D. ODay, G. Carichner, E. Marsman, N. Nguyen, S. Kubba, S. Nguyen, J. Kuhn, and R. B. Brown, "A 0.5-to-480 MHz self-referenced CMOS clock generator with 90 ppm total frequency error and spread-spectrum capability," in *Proc. IEEE ISSCC*, San Francisco, CA, Feb. 3–7, 2008, pp. 350–351.

Gavin K. Ho (S'02–M'07) received the B.A.Sc. and M.Eng. degrees in mechanical engineering from The University of British Columbia (UBC), Vancouver, Canada, and the M.S. and Ph.D. degrees in electrical and computer engineering from the Georgia Institute of Technology (Georgia Tech), Atlanta.

In 1999, he was a Junior Opto-Mechanical Design Engineer with Creo Products, Inc. (currently part of Eastman Kodak Company). From 2000 to 2001, he was an Electro-Mechanical Design Engineer with Pelton Reforestation Ltd. (currently part of Pacific Regeneration Technologies, Inc.). From 2005 to 2006, he taught undergraduate electrical engineering courses at Georgia Tech. He was a Process Development Engineer with Analog Devices, Inc., Cambridge, MA, from 2006 to 2008. He is currently the President of ParibX, Inc., Mountain View, CA. His interests include MEMS manufacturing and process integration; device design and system performance analysis; and strategic marketing of RF MEMS, optical MEMS, sensors, reference oscillators, and emerging technologies.

Dr. Ho received the Letson Prize from UBC for graduating at the top of the class in mechanical engineering. He also received the Col. Oscar P. Cleaver Award from Georgia Tech for placing first in the Ph.D. examination in electrical engineering in spring 2002. He was a recipient of the Woodruff Fellowship and the N. Walter Cox Fellowship at Georgia Tech. Six of the issued and pending U.S. patents from his Ph.D. research are licensed to three entities in the semiconductor industry.

Krishnakumar Sundaresan (S'98–M'07) was born in Chennai (Madras), India, in 1980. He received the B.E. degree in electrical and electronics engineering from the University of Madras, Chennai, in 2001, and the Ph.D. degree in electrical and computer engineering from the Georgia Institute of Technology (Georgia Tech), Atlanta, in 2006.

He is currently a System-on-Chip Designer with GE Global Research, Niskayuna, NY. His research interests are in the area of analog circuit design and include interface circuits for medical detectors, circuits for MEMS-based frequency references, and process–voltage–temperature-tolerant circuit design.

Dr. Sundaresan was a recipient of the 2005 Analog Devices–Georgia Tech Student Analog Designer of the Year Award.

Siavash Pourkamali (S'02–M'06) received the B.S. degree in electrical engineering from Sharif University of Technology, Tehran, Iran, in 2001, and the M.S. and Ph.D. degrees from the Georgia Institute of Technology (Georgia Tech), Atlanta, in 2004 and 2006, respectively.

He is currently an Assistant Professor in the Department of Electrical and Computer Engineering, University of Denver, Denver, CO. His main research interests are in the areas of integrated silicon MEMS and microsystems, micromachining technologies, RF MEMS resonators and filters, and nanomechanical resonant sensors.

Dr. Pourkamali was a recipient of the 2005 Georgia Tech Sigma Xi Best M.S. Thesis Award and the 2006 Georgia Tech Electrical and Computer Engineering Research Excellence Award. He was also a silver medal winner at the 29th International Chemistry Olympiad (IChO). He is a holder several patents in the areas of silicon micro-/nanomechanical resonators and filters and nanofabrication technologies.

Farrokh Ayazi (S'96–M'00–SM'05) received the B.S. degree in electrical engineering from the University of Tehran, Tehran, Iran, in 1994, and the M.S. and Ph.D. degrees in electrical engineering from the University of Michigan, Ann Arbor, in 1997 and 2000, respectively.

He joined the faculty of the Georgia Institute of Technology (Georgia Tech), Atlanta, in December 1999, where he is currently a Professor in the School of Electrical and Computer Engineering (ECE). His research interests are in the areas of integrated micro- and nanoelectromechanical resonators, IC design for MEMS and sensors, RF MEMS, inertial sensors, and microfabrication techniques.

Dr. Ayazi is a recipient of a 2004 NSF CAREER Award, the 2004 Richard M. Bass Outstanding Teacher Award (determined by the vote of the ECE senior class), and the Georgia Tech College of Engineering Cutting Edge Research Award for 2001–2002. He is an Editor for the JOURNAL OF MICROELECTROMECHANICAL SYSTEMS. He served on the Technical Program Committee of the IEEE International Solid-State Circuits Conference for six years (2004–2009). He is the Co-Founder and Chief Technical Officer of Qualtré Inc., a spin-out from his research Laboratory that commercializes multi-axis microgyroscopes based on silicon bulk acoustic wave (BAW) technology for consumer electronics and personal navigation systems.